Supporting Information for

Amplified Risk of Compound Heat Stress -Dry Spells in Urban India

Poulomi Ganguli[1]

[1]Agricultural and Food Engineering Department, Indian Institute of Technology Kharagpur, India

[*]Corresponding author: P. Ganguli (pganguli@agfe.iitkgp.ac.in)

S1.1 Determination of Average Timing of Extreme Temperature

The time to extreme temperature (*i.e.*, annual maxima temperature) is analyzed using directional statistics (Mardia 1975), which is widely used method to define the timing of extreme peak discharge and extreme precipitation events respectively (Dhakal et al. 2015; Blöschl et al. 2017), however, hardly in use for detecting timing of heatwaves or droughts. The date, D_i (Julian day) of occurrence of annual maxima temperature is converted to an angular value, θ_i (in radians) using the following expression (Laaha and Blöschl 2006)

$$\theta_i = D_i \frac{2\pi}{L} \tag{S1}$$

Where, i shows the peak discharge events, D indicates Julian dates ranging from 1 to 365 or 366 days based on leap or a non-leap year; L denotes the number of days in a calendar year. For n extreme temperature events, the mean annual maxima temperature date is calculated using the weighted average of the sampled extremes, weighing the individual annual maxima daily mean temperature value, T_i, where i = 1, …., n, the length of the sampled extremes (Burn and Whitfield 2018)

$$\bar{x} = \frac{\sum_{i=1}^{n} T_i \cos\theta_i}{\sum_{i=1}^{n} T_i}; \bar{y} = \frac{\sum_{i=1}^{n} T_i \sin\theta_i}{\sum_{i=1}^{n} T_i} \tag{S2}$$

Where, $\bar{x}$ and $\bar{y}$ denote the x- and y-coordinates of the mean event date. The occurrence time of the extreme temperature is derived from mean direction, $\bar{\theta}$, where θ_1, ….., θ_n are the individual event dates expressed to an angular value (from Eq. S1).

$$\bar{\theta} = \begin{cases} \tan^{-1}\left(\frac{\bar{y}}{\bar{x}}\right) \; if\ \bar{x} > 0\, and\ \bar{y} > 0 \\ 180 - \tan^{-1}\left(\frac{\bar{y}}{\bar{x}}\right) \; if\ \bar{x} < 0\, and\ \bar{y} > 0 \\ 180 + \tan^{-1}\left(\frac{\bar{y}}{\bar{x}}\right) \; if\ \bar{x} < 0\, and\ \bar{y} < 0 \\ 360 + \tan^{-1}\left(\frac{\bar{y}}{\bar{x}}\right) \; if\ \bar{x} > 0\, and\ \bar{y} < 0 \\ \pi/2 \;\; if\ \bar{x} = 0\ and\ \bar{y} > 0 \\ 3\pi/2\ if\ \bar{x} = 0\ and\ \bar{y} < 0 \end{cases} \tag{S3}$$

Finally, the mean occurrence date, ϖ of extreme temperature is computed as

$$\varpi = \bar{\theta} \times \left(\frac{L}{2\pi} \right) \tag{S4}$$

The temporal variability in the timing of occurrence of extreme temperature is calculated using circular variance

$$s^2 = -2\log\left(\bar{R}\right) \tag{S5}$$

Where, $\bar{R} = \sqrt{\bar{x}^2 + \bar{y}^2}$ (S6)

S1.2 Modelling Upper and Lower Tail Dependence Between Compound Drivers

The (lower) upper tail correlation, λ_{CFG} is estimated using the following expression (Poulin et al. 2007)

$$\hat{\lambda}_{CFG} = 2 - 2\exp\left\{ \frac{1}{n} \sum_{i=1}^{n} \log\left[\sqrt{\log\left(\frac{1}{u_i}\right)\log\left(\frac{1}{v_i}\right)} \middle/ \log\left(\frac{1}{\max\left(u_i, v_i\right)^2} \right) \right] \right\} \tag{S7}$$

Where, u_i and v_i denote the empirical cumulative distributions of inter-dependent pairs and n is the sample length. The empirical cumulative distribution is determined using, $F_X^{[e]}\left(x\right) = \sum_{i=1}^{n} I_k \middle/ n$, where $I_k\left(\Omega\right)$ is the logical indicator function of set Ω, taking the value of either 1 (if Ω is true) or 0 (if Ω is false). While for lower tail dependence, the data are arranged in descending order, $x_i \geq x_k$; for the upper tail dependence, the data are arranged in ascending order, $x_i \leq x_k$ to evaluate the rank of the data.

S1.3 Extreme Value Theory to Model Compound Drivers

The block maxima approach defines a statistical model for $Z_t = \max\left\{Y_{t,1}, ..., Y_{t,n}\right\}$, where $\left\{Y_{t,i}, i = 1, ..., n\right\}$ are daily climatological records (*e.g.*, mean daily temperature) within a "block" *t* (*e.g.*, average heatwave intensity and wind speed during the 10-day time window in each year). The cumulative distribution (CDF) of GEV distribution is expressed as below (Coles et al. 2001)

$$G(x)=\begin{cases}\exp\left\{-\left[1+\xi\left(\dfrac{x-\mu}{\sigma}\right)\right]_{+}^{-\frac{1}{\xi}}\right\} & if\ \xi\neq 0\\ \exp\left\{-\exp\left(-\dfrac{x-\mu}{\sigma}\right)_{+}\right\} & if\ \xi\to 0\end{cases}\tag{S8}$$

Where, $y_{+}=\max\{y,0\}$ with '+' shows the non-negative part of *y*, the parameters, μ, σ and ξ indicates the location, scale and shape parameters of stationary form GEV distribution.

S1.4 Kendall's Distribution Function and Its Estimation

The Kendall distribution function, $K_C(t)$ helps to project multivariate information into a single dimension using a *d*-dimensional copula distribution, $\boldsymbol{F}=C(\boldsymbol{U})$ with a critical probability level, $\overline{p}_t$ (Salvadori et al. 2013)

$$\overline{p}_t=\left\{\boldsymbol{F}(\boldsymbol{X})=t,\ \boldsymbol{X}\in\boldsymbol{R}^d\right\}\qquad \text{where } t\in(0,1]\tag{S9}$$

Thus $\overline{p}_t$ is the iso-surface with dimension *d*-1 for the trivariate distribution, $\overline{p}_t$ partitions $\boldsymbol{R}^d$ into three non-overlapping regions: the sub-critical region consisting of points that are less than $\overline{p}_t$; the critical layer $\overline{p}_t$, where $\boldsymbol{F}$ equals the constant value *t*; the super-critical region consisting of points that are greater than that of $\overline{p}_t$. The probability of a supercritical event for a set of realizations can be computed using the Kendall distribution function, $K_C(t)$. The Kendall's distribution function, K_C is obtained numerically using the following steps:

- Generate a random samples $\mathbf{X}_1^*,\ldots,\mathbf{X}_m^*$, where, *m* = length of simulated samples from the copula *C*, *n* = observed sample length, and $m\geq n$, then compute their associated rank vectors $\mathbf{R}_1^*,\ldots,\mathbf{R}_m^*$
- Compute the transformed data $V_i^*=\dfrac{1}{m}\sum_{j=1}^{m}\mathbf{1}\left(\mathbf{R}_j^*\leq\mathbf{R}_i^*\right)=\dfrac{1}{m}\sum_{j=1}^{m}\prod_{l=1}^{d}\mathbf{1}\left(R_{jl}^*\leq R_{il}^*\right),\quad j\in\{1,\ldots,m\}$ for every $\boldsymbol{R}=\{R_1,\ldots,R_d\}$
- Approximate $K_C(.)$ by $K_{C_U}(t)=\dfrac{1}{m}\sum_{i=1}^{m}\mathbf{1}\left(V_i^*\leq t\right),\qquad t\in[0,1]$

S1.5 Modelling Vertically Integrated Moisture Transport

The daily instantaneous dataset of zonal (IVT_u) and meridional (IVT_v) water vapor flux (in kgm^{-1}s^{-1}) dataset is obtained from the European Centre for Medium-Range Weather Forecasts (ECMWF) Interim Reanalysis (ERA-interim) archive (https://apps.ecmwf.int/datasets/data/interim-full-daily/levtype=sfc/) at a spatial resolution of 0.75°. The archived dataset from ERA-interim shows credible representation of moisture transport over the tropics (Knippertz et al. 2013; Pathak et al. 2017). IVT_u and IVT_v are calculated from 2-dimensional pressure-level data between 1000 and 300 hPa (Champion et al. 2015). The magnitude (*i.e.*, composite) and direction of IVT_u and IVT_v at each grid level is computed using the following expression (Brands et al. 2017):

$$IVT = \sqrt{IVT_u^2 + IVT_v^2} \tag{S10}$$

$$D = atan2\left(\frac{IVT_u}{IVT}, \frac{IVT_v}{IVT}\right)\frac{180}{\pi} + 180 \tag{S11}$$

Where *IVT* and *D* are magnitude and direction of the vertical integrals of the zonal and meridional water vapor transport components respectively. The *atan2* function returns the four-quadrant inverse tangent ranging from $-\pi$ to π, which is then transformed to degree values ranging between 0° and 360°. Finally, to evaluate synoptic scale water vapor transport anomaly, the standardized anomaly of *IVT* (SA_{IVT}) is computed for each grids as follows (Hart and Grumm 2001):

$$SA_{IVT} = \frac{IVT_i - \overline{IVT}}{\sigma_{IVT}} \tag{S12}$$

Where, IVT_i is the magnitude of *IVT* on the day of occurrence of maximum temperature (see Figure 2b), $\overline{IVT}$ and σ_{IVT} represent long-term average and standard deviation values respectively, and obtained from daily magnitude of vertically integrated moisture transport for the period (1979-2017; the ERA-interim dataset is available from 1979 onwards).

Table S1. List of sites and period of record availability

Sr. #	Station ID	Location	Population (Million)	Available record
1	42111	Dehradun	0.53	1970 - 2017
2	42182	New Delhi	12.88	1970-2018
3	42410	Guwahati	0.82	1970 - 2017
4	42647	Ahmedabad	4.53	1970-2017
5	42754	Indore	1.52	1970-2016
6	42809	Kolkata	13.21	1970-2018
7	42971	Bhubaneshwar	0.66	1970-2018
8	43003	Mumbai	16.43	1970-2018
9	43128	Hyderabad	5.74	1970-2017
10	43192	Panjim	0.10	1970-2016
11	43279	Chennai	6.56	1970-2017
12	43296	Bengaluru	5.70	1970-2017
13	43321	Coimbatore	1.46	1970-2017
14	43372	Thiruvananthapuram	0.89	1970-2017
15	42131	Hissar	0.26	1970-2017
16	42165	Bikaner	0.53	1970-2017
17	42369	Lucknow/Amausi	2.25	1970-2017
18	42492	Patna	1.70	1970-2009
19	42701	Ranchi	0.86	1970-2016
20	42867	Nagpur	2.13	1970-2016
21	42875	Raipur	0.70	1970-2012
22	43149	Visakhapatnam	1.35	1970-2016
23	43201	Gadag	0.15	1970-2017

Table S2. Trends in compound drought driver

Station ID	HWI (°C)			Low Wind speed (Km h^{-1})			Precipitation Deficit (mm)		
	MK-Statistics	p-value	Slope (%change/decade)	MK-Statistics	p-value	Slope (%change/decade)	MK-Statistics	p-value	Slope (%change/decade)
42111	1.33	0.18	0.52	-1.20	0.23	*0.0*	0.27	0.78	0.73
42182	-0.32	0.74	-0.30	-0.97	0.33	-5.35	-0.45	0.65	*0.0*
42410	**2.74**	**0.006***	**1.26**	**-2.31**	**0.02**	**-35.16**	0.17	0.86	0.51
42647	1.65	**0.098**	0.65	-0.28	0.78	*0.0*	-0.22	0.82	*0.0*
42754	-0.35	0.72	-0.13	**-3.0**	**0.003**	**-20.21**	0.29	0.77	*0.0*
42809	**3.12**	**0.002**	**1.32**	**-2.81**	**0.005**	**-24.18**	-1.36	0.17	-4.01
42971	0.82	0.41	0.38	-1.90	**0.06**	-18.18	0.68	0.50	7.0
43003	1.35	0.17	0.59	**-3.30**	**0.001**	**-12.0**	1.11	0.27	*0.0*
43128	**1.97**	**0.048**	**0.44**	**-2.07**	**0.039**	**-10.83**	0.53	0.60	*0.0*
43192	**2.0**	**0.045**	0.55	**-2.59**	**0.01**	**-26.13**	0.27	0.78	*0.0*
43279	-1.61	0.106	-0.37	**-3.33**	**0.001**	**-13.12**	0.73	0.46	*0.0*
43296	**2.45**	**0.014**	0.62	**-2.08**	**0.038**	**-9.11**	0.47	0.64	*0.0*
43321	1.57	0.12	0.54	**-2.29**	**0.022**	**-11.95**	-0.87	0.39	-1.6
43372	**2.10**	**0.035**	**0.39**	**-2.02**	**0.04**	**-10.9**	-1.58	0.11	-8.23
42131	0.65	0.52	-0.45	**-2.52**	**0.012**	**-16.4**	1.51	0.13	11.58
42165	1.49	0.14	0.55	-0.51	0.61	*0.0*	-1.56	0.12	*0.0*
42369	0.62	0.53	1.02	1.15	0.25	37	0.59	0.55	*0.0*
42492	0.80	0.42	0.36	0.19	0.85	*0.0*	-0.86	0.39	*0.0*
42701	0.42	0.67	0.54	**-2.9**	**0.004**	**-36**	-0.93	0.35	-4.8
42867	1.91	**0.056**	0.46	**-3.31**	**0.001**	**-20.37**	-0.23	0.82	*0.0*
42875	-0.49	0.62	-0.45	**-2.44**	**0.015**	**-13.16**	0.79	0.43	12.3
43149	1.53	0.13	0.83	**-3.52**	**<0.05**	**-33.6**	-1.48	0.14	-7.55
43201	0.90	0.37	0.21	-0.43	0.66	*0.0*	-1.43	0.15	-9.46

*The fonts in bold indicate changes decade^{-1} is statistically significant at 10% level. The fonts in italics show no changes. The largest significant decrease in wind speed is shown in a red font.

Table S3. Marginal distribution fit of HWI

Station ID	GEV Model*	GEV parameter			KS-statistics (d)	p-value
		Location	Scale	Shape		
42111	GEV_t -0	29.17	1.30	-0.30	0.108	0.63
42182	GEV_t -0	33.80	1.99	-0.30	0.107	0.62
42410	GEV_t - I	29.0 -0.18t	1.07	-0.35	0.112	0.54
42647	GEV_t –I	34.41-1.14t	1.15	-0.30	0.075	0.94
42754	GEV_t -0	32.97	1.09	-0.32	0.072	0.96
42809	GEV_t – I	31.28 + 0.56t	1.36	-0.23	0.085	0.85
42971	GEV_t -0	32.39	1.37	-0.27	0.124	0.49
43003	GEV_t -0	30.05	1.01	-0.40	0.092	0.82
43128	GEV_t – I	33.74 + 2.09t	1.09	-0.26	0.094	0.76
43192	GEV_t -I	30.06+0.51t	0.76	-0.41	0.136	0.41
43279	GEV_t -0	33.87	0.92	-0.25	0.097	0.73
43296	GEV_t – I	27.87 + 1.18t	0.70	-0.19	0.083	0.87
43321	GEV_t -0	30.05	0.97	-0.30	0.074	0.95
43372	GEV_t – I	29.33 + 0.82t	0.46	-0.16	0.112	0.59
42131	GEV_t -0	34.69	1.61	-0.20	0.181	0.99
42165	GEV_t – 0	35.91	1.80	-0.59	0.144	0.32
42369	GEV_t -0	32.41	2.60	-0.60	0.136	0.76
42492	GEV_t -0	32.62	1.12	-0.16	0.142	0.39
42701	GEV_t -0	30.9	1.50	-0.35	0.096	0.86
42867	GEV_t – I	36.31 – 0.13t	1.41	-0.60	0.074	0.94
42875	GEV_t -0	35.35	1.85	-0.70	0.146	0.54
43149	GEV_t -0	32.76	1.36	-0.32	0.065	0.98
43201	GEV_t -0	29.82	1.01	-0.44	0.170	0.15

*GEV: Generalized Extreme Value distribution with stationary (GEV_t -0) and nonstationary (GEV_t – I) form with nonstationarity in location parameter. The p-value > 0 indicates the stationary/nonstationary GEV model fits the data reasonably well.

Table S4. Marginal distribution fit of low wind speed

Station ID	GEV Model*	GEV parameter			KS-statistics (*d*)	p-value
		Location	Scale	Shape		
42111	GEV_t -0	1.91	0.95	-0.20	0.284	0.001
42182	GEV_t -0	4.12	2.10	-0.05	0.114	0.533
42410	GEV_t – I	0.65+0.28t	0.91	0.16	0.19	0.045
42647	GEV_t -0	5.27	1.71	0.04	0.112	0.58
42754	GEV_t – I	7.66 + 9.72t	4.12	-0.19	0.071	0.97
42809	GEV_t – I	3.96+0.29t	2.20	-0.04	0.10	0.67
42971	GEV_t – I	5.37 -0.21t	3.16	-0.017	0.127	0.46
43003	GEV_t – I	5.84 - 0.09t	1.67	-0.32	0.18	0.10
43128	GEV_t – I	5.94+0.032t	2.43	-0.12	0.09	0.84
43192	GEV_t – I	6.32 -0.064t	2.85	-0.41	0.158	0.24
43279	GEV_t – I	7.69 - 0.72t	2.02	-0.23	0.14	0.28
43296	GEV_t – I	4.15 - 0.87t	1.65	-0.25	0.17	0.12
43321	GEV_t – I	4.96 +0.19t	1.99	-0.11	0.15	0.24
43372	GEV_t – I	3.53 + 0.26t	2.01	-0.21	0.14	0.30
42131	GEV_t – I	2.96 – 1.09t	1.05	0.21	0.20	0.05
42165	GEV_t -0	3.46	2.24	0.34	0.13	0.44
42369	GEV_t -0	1.78	1.77	0.01	0.19	0.33
42492	GEV_t -0	2.01	1.49	-0.06	0.14	0.44
42701	GEV_t – I	4.08 – 0.58t	2.66	-0.24	0.11	0.70
42867	GEV_t – I	5.30 – 0.53t	2.32	-0.09	0.16	0.17
42875	GEV_t – I	4.14+4.37t	1.29	-0.07	0.18	0.26
43149	GEV_t – I	3.27 - 1.04t	2.51	-0.12	0.12	0.53
43201	GEV_t – I	7.17	2.78	-0.45	0.17	0.16

Table S5. Marginal distribution fit of precipitation deficit

Station ID	Selected distribution	AICc Lognormal	AICc Loglogistic	AICc Gamma	AICc GEV
42111	Log logistic	-238.29	**-256.38**	-245.06	-236.9
42182	Gamma	-162.8	-166.05	**-168.13**	-159.14
42410	GEV	-217.61	-256.01	-279.92	**-312.6**
42647	Gamma	-39.67	-39.30	**-39.80**	-33.75
42754	Gamma	-80.18	-79.88	**-80.64**	-71.09
42809	Gamma	-217.08	-228.09	**-244.64**	-228.75
42971	Gamma	-164.70	-176.7	**-186.4**	-171.49
43003	Log logistic	-48.06	**-48.34**	-48.06	-42.52
43128	Gamma	-107.64	-110.89	**-110.94**	-105.12
43192	Gamma	-110.39	-110.23	**-112.02**	-96.29
43279	Gamma	-108.14	-107.91	**-111.8**	-98.43
43296	Gamma	-158.73	-166.03	**-167.85**	-154.11
43321	Gamma	-144.5	-155.46	**-156.25**	-152.84
43372	GEV	-172.98	-186.51	-196.8	**-206.95**
42131	Gamma	-124.89	-127.89	**-129.26**	-120.17
42165	Gamma	-61.5	-61.91	**-62.31**	-55.86
42369	Gamma	-32.5	-32.55	**-33.63**	-27.18
42492	Log logistic	-69.14	**-70.73**	-70.65	-64.05
42701	Gamma	-133.55	-135.2	**-138.3**	-130.34
42867	Gamma	-105.63	-105.91	**-108.83**	-96.04
42875	Gamma	-104.19	-104.72	**-108.44**	-93.54
43149	Gamma	-184.68	-190.8	**-203.09**	-170.46
43201	Gamma	-152.07	-162.11	**-163.82**	-151.45

*****In bold font shows the best fitting distribution with minimum AIC values with small sample correction.

Table S6. Degrees of freedom parameter and the performance of trivariate student's *t* copula

Station ID	Degrees of Freedom	p-value*
42111	5	0.54
42182	3	0.24
42410	5	0.95
42647	9	0.47
42754	10	0.93
42809	10	0.14
42971	2	0.28
43003	2	0.57
43128	4	0.25
43192	7	0.29
43279	5	0.40
43296	10	0.06
43321	8	0.21
43372	10	0.02
42131	8	0.86
42165	5	0.11
42369	3	0.38
42492	6	0.50
42701	3	0.012
42867	4	0.29
42875	6	0.39
43149	8	0.028
43201	5	0.692

*p-values of student's *t* copula is obtained using parametric bootstrap-based approach using $N = 250$ bootstrap sample.

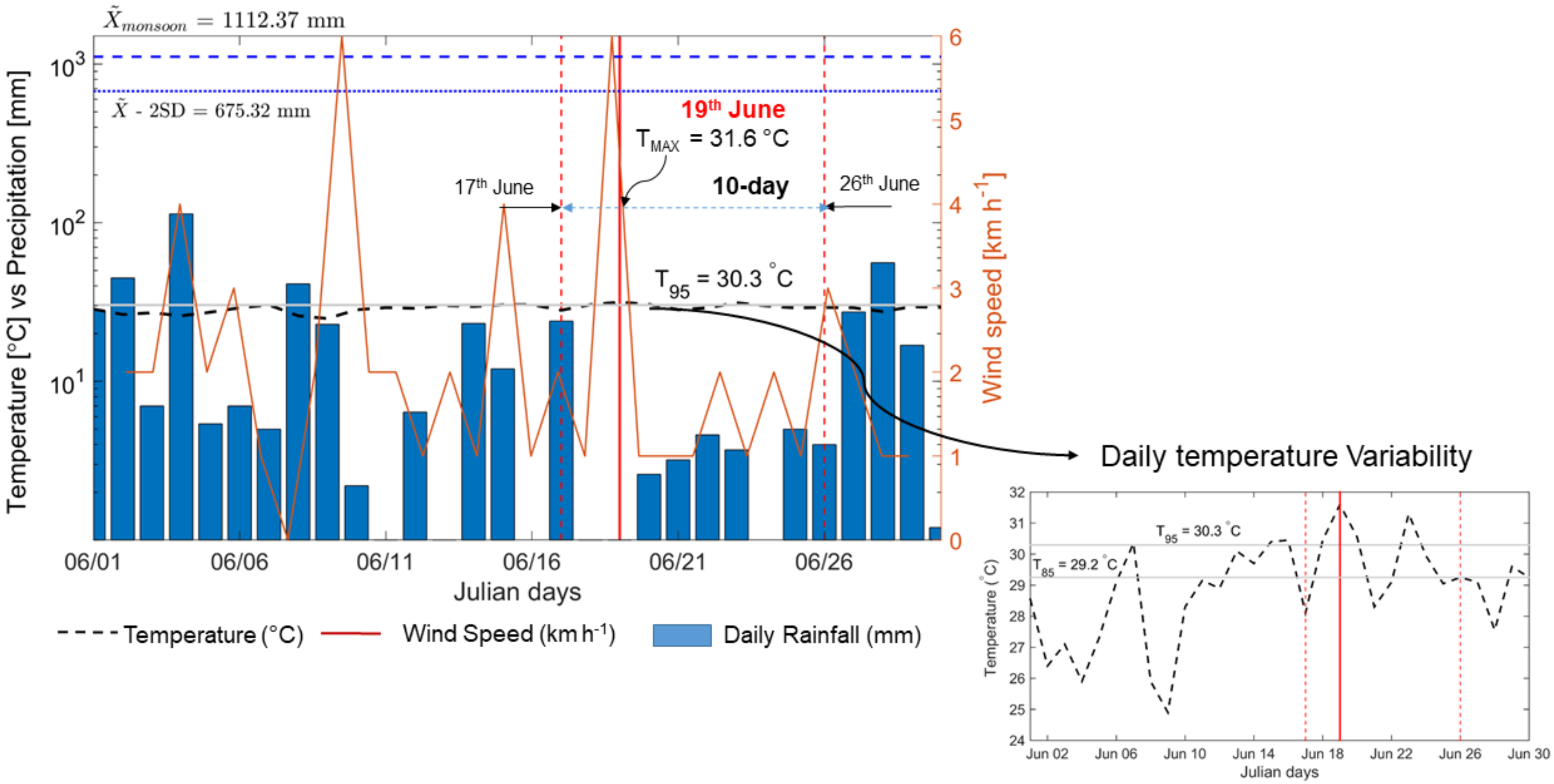

Figure S1. Same as Figure 2(a) but for humid tropical region (Guwahati city). The horizontal dashed line (parallel to x-axes) in blue shows seasonal climatology of monsoon (June – September) precipitation. Dotted line in blue shows -2 SD departure from mean monsoon rainfall. The inset shows the daily temperature variability, the maximum temperature and the temperature during surrounding days of the maximum temperature. The horizontal lines (in gray), parallel to the x-axis show the temperature percentiles, calculated from the daily temperature records.

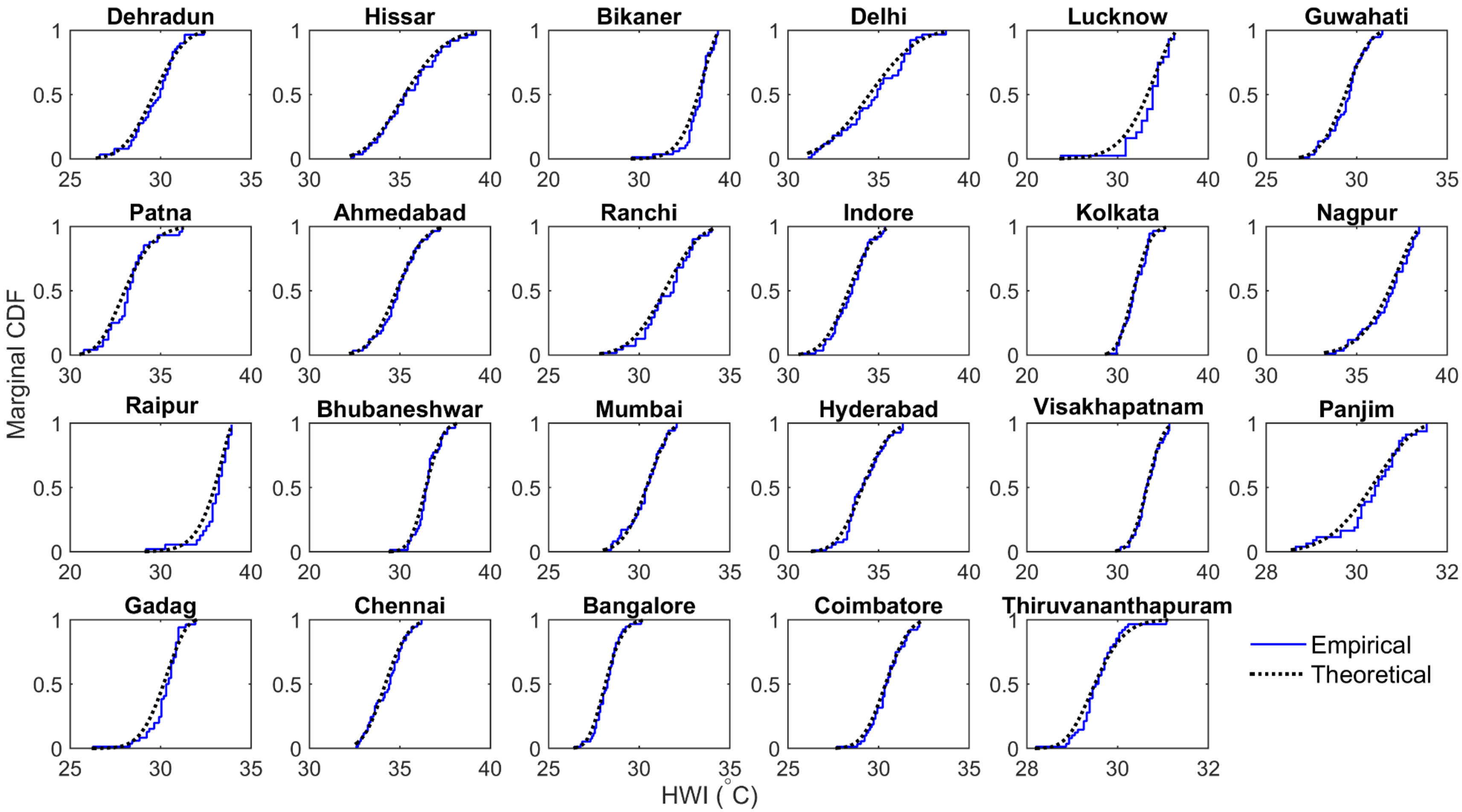

Figure S2. Marginal distribution fit of heatwave intensity (HWI, in °C). The CDF plots of empirical versus theoretical distributions are compared across all urban locations.

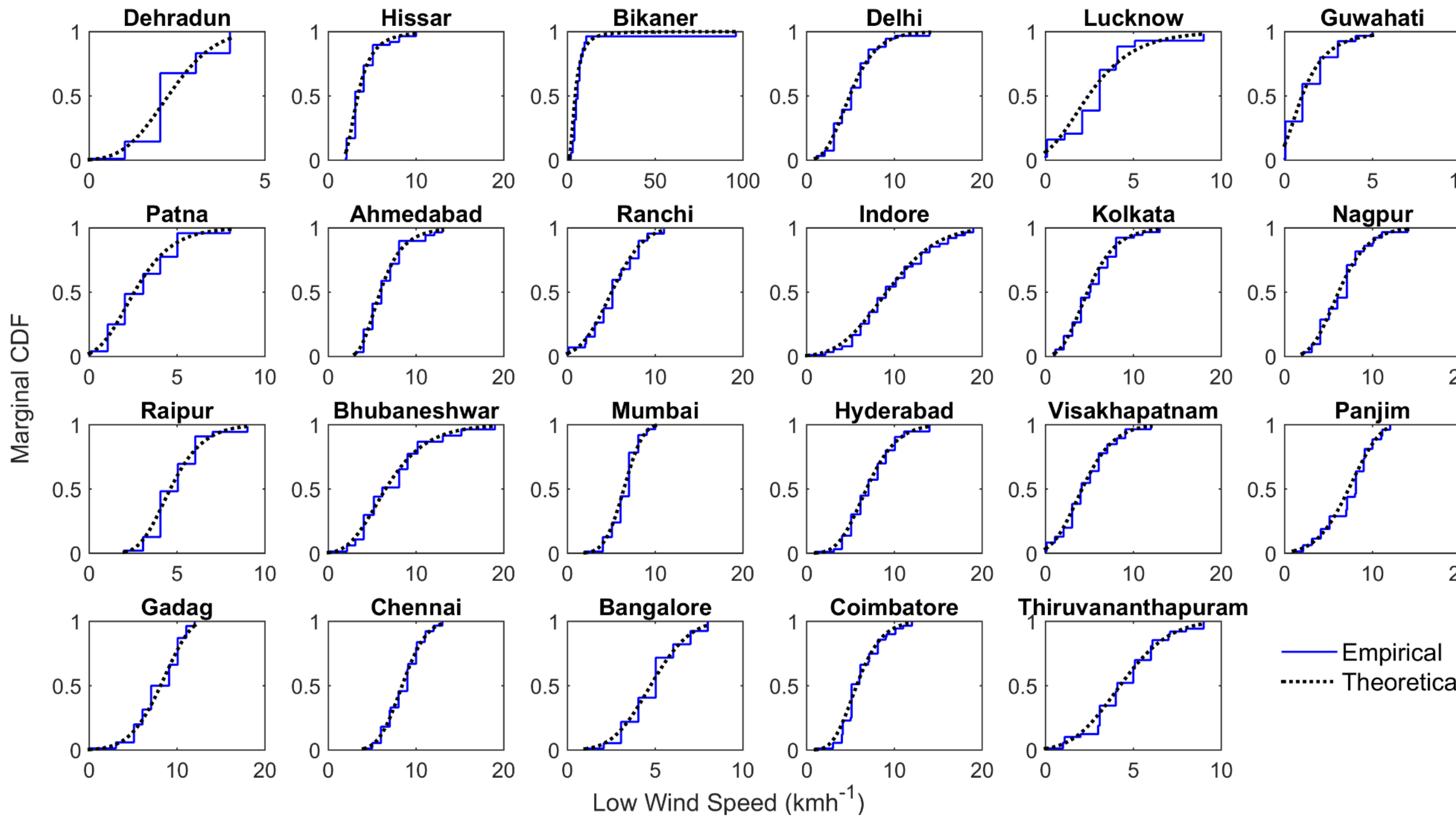

Figure S3. Marginal distribution fit of low wind speed (in kmh^{-1}). The CDF plots of empirical versus theoretical distributions are compared across all urban locations.

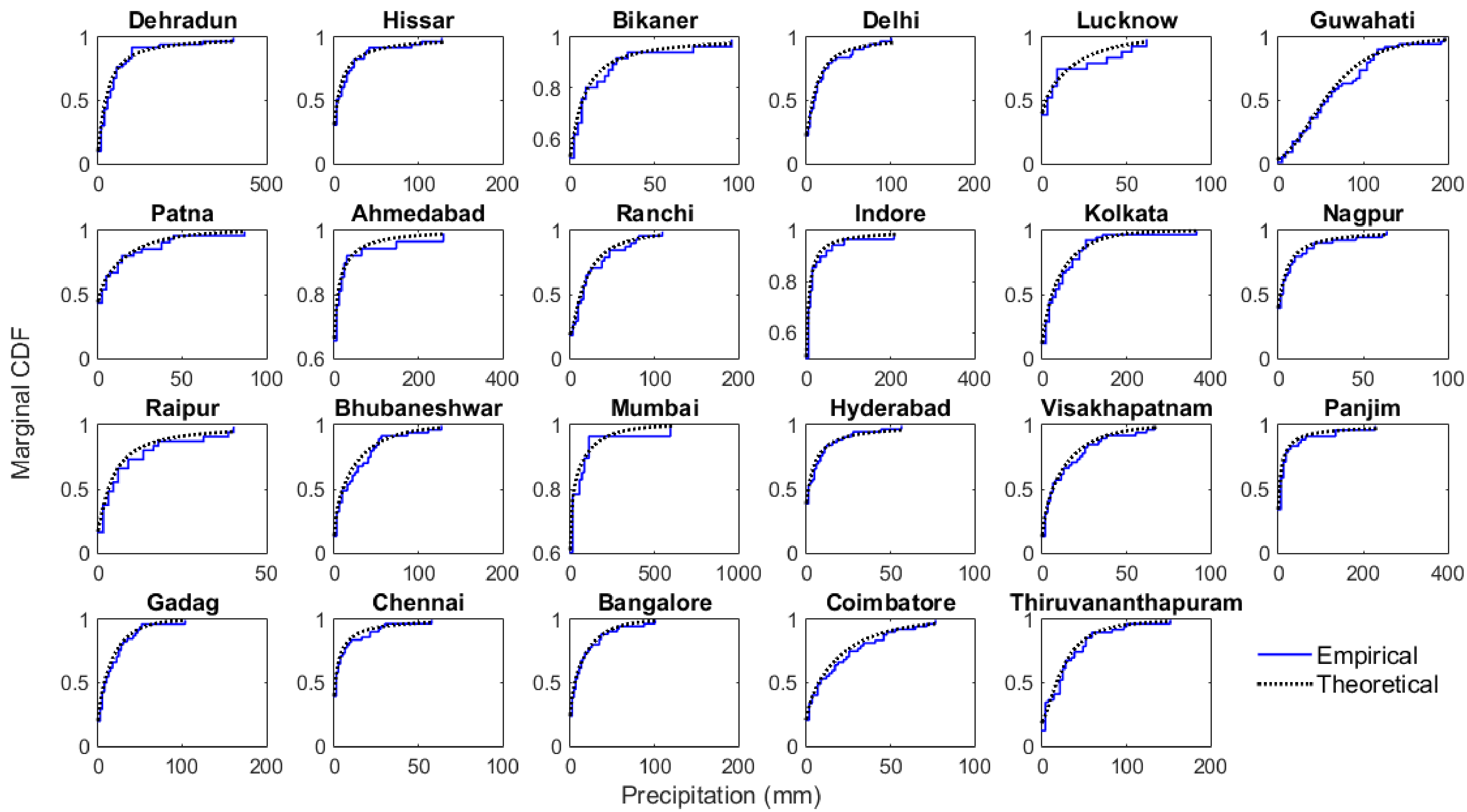

Figure S4. Marginal distribution fit of precipitation (in mm). The CDF plots of empirical versus theoretical distributions are compared across all urban locations.

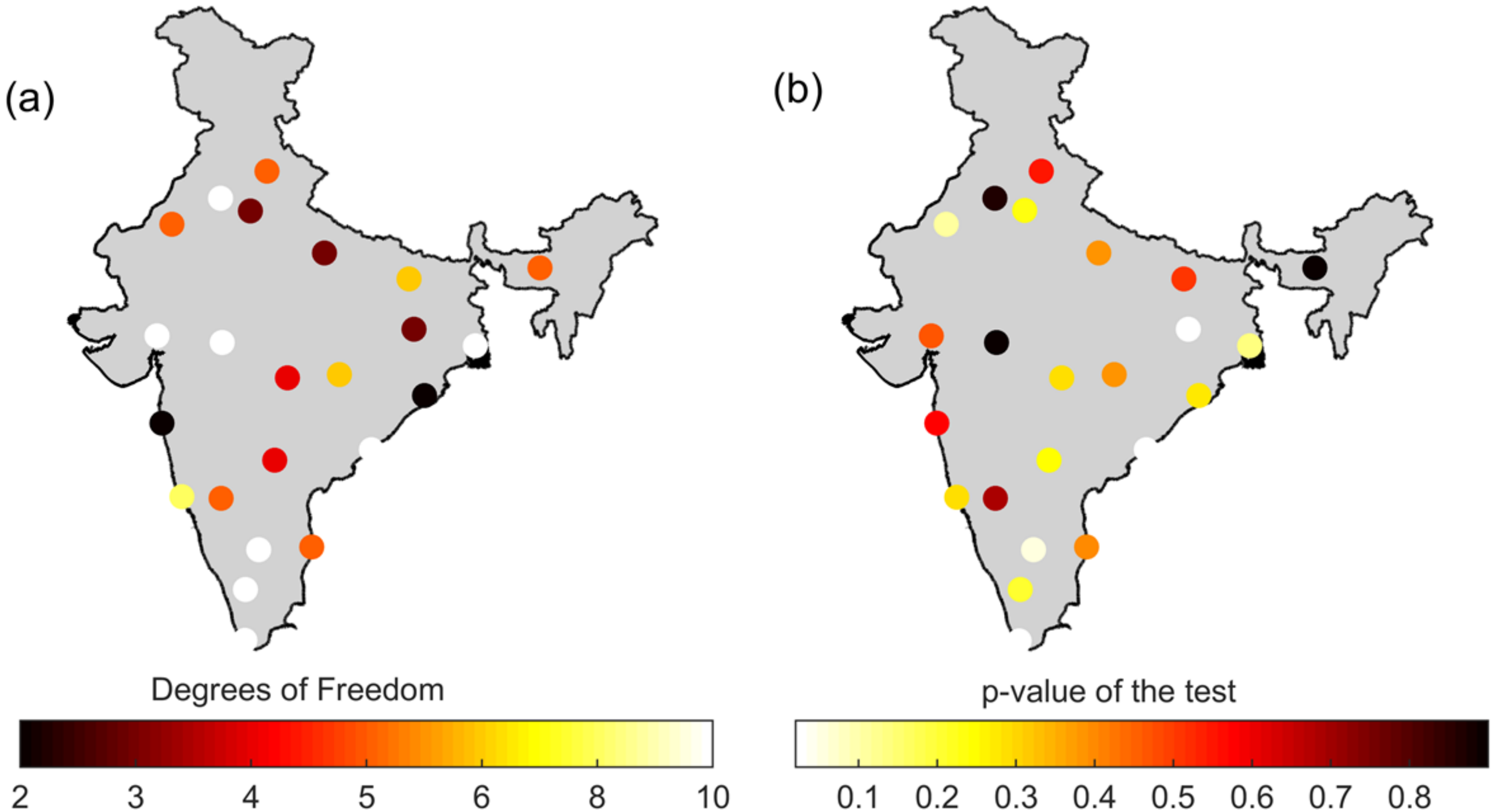

Figure S5. Spatial variability in degrees of freedom parameter and the probability of obtaining test result for trivariate Student's *t* copula. (a) Degrees of freedom of the fitted Student's *t* copula across urban sites. The dark shades indicate lower degrees of freedom, whereas lighter shades suggest higher degrees of freedom. (b) The probability value (p-value) of the test, obtained from N = 250 bootstrap iterations of the parametric bootstrap approach for assessing the goodness-of-fit of copula models.

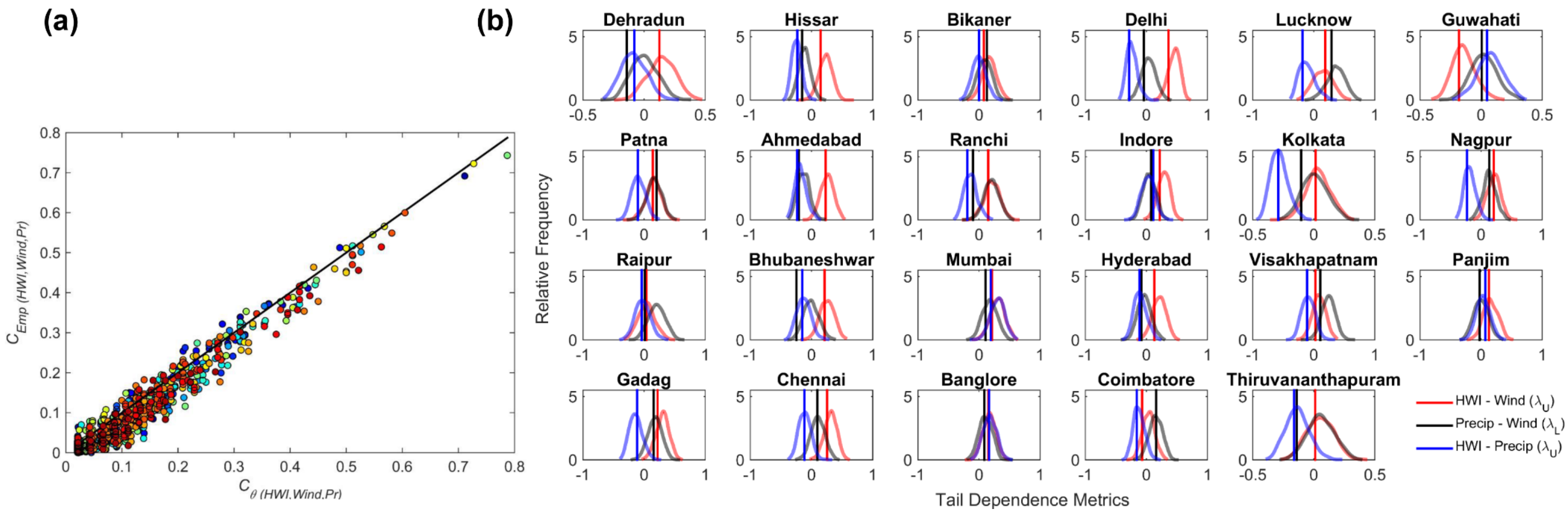

Figure S6. Assessing Fit of the trivariate Student's *t* copula model. (a) Empirical versus Student's *t* copula with varying degrees of freedom. The circles in shades close to 1:1 scatter show the fitted copula model over 23 urban locations, each shade representing the individual urban site. (b) Observed (vertical lines) versus density functions of simulated tail dependences for three dependence pairs, HWI-low wind (in red), dry spell – low wind (in black), and HWI-dry spell (in blue). The dependence of HWI-low wind speed, and HWI-precipitation deficit pairs are shown using the upper tail dependence (λ_U), whereas the dependence of precipitation deficit-versus-low wind speed are shown using the lower tail dependence (λ_L). The trends in simulated tail dependences are analogous to observed trends in that they encompass the overall pattern together with uncertainty in the estimation.

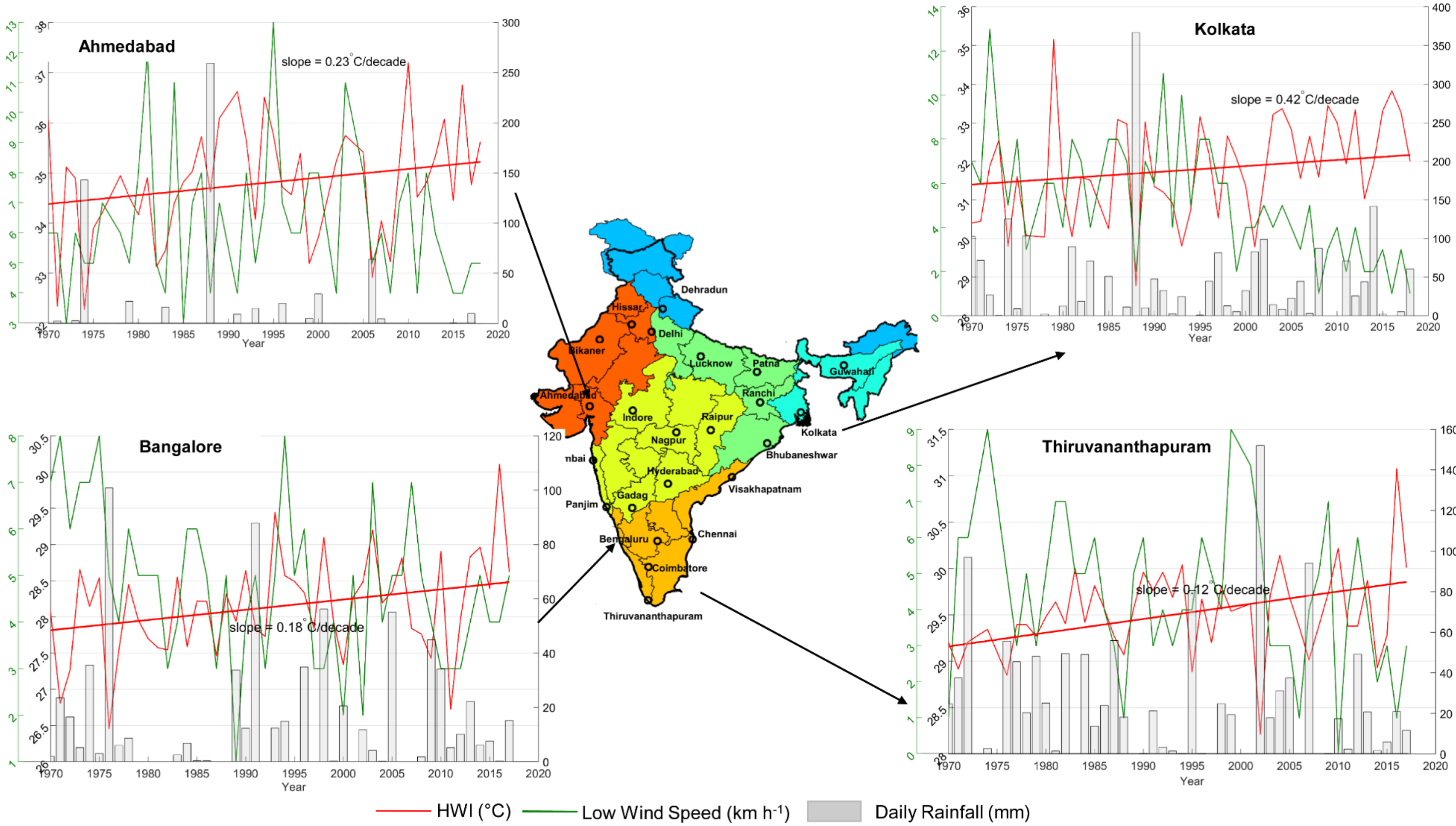

Figure S7. The trend in heatwaves across selected urban locations located across hydroclimatologically disparate regions of the country. The solid red lines show the fitted (linear) trend. The slope (per decade) is calculated using non-parametric Theil-Sen's method, which is shown against the least-square regression line. The largest increasing trend is observed for Kolkata, which is located at the northeast climate region.

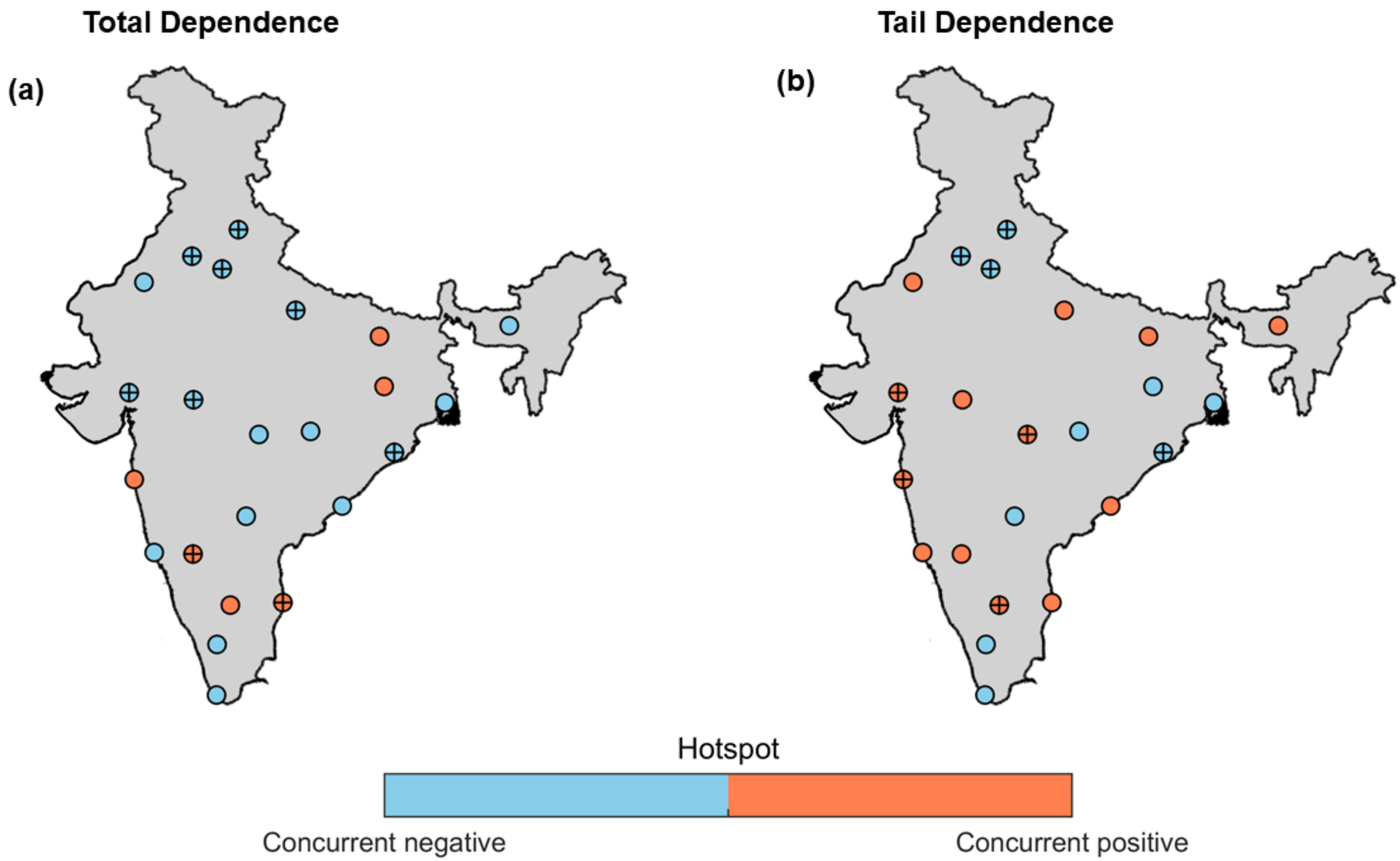

Figure S8. Spatial variability in concomitance among dependence pairs. Shades in circles show when two or more dependence pairs show analogous signs, *i.e.*, they exhibit concomitance. Stippling ('+') is shaded when 2 out of three or all dependence pairs show significant dependence at 10% significance level, indicating agreement in dependence strengths among pair-wise variables. None of the pair-wise variables show independence (or zero correlations). The shades of circles in blue indicate when two or more dependence pairs show negative dependence. Conversely, the circles in orange show when two or more dependence pairs show positive dependence.

References

Blöschl G, Hall J, Parajka J, et al (2017) Changing climate shifts timing of European floods. Science 357:588–590

Brands S, Gutiérrez JM, San-Martín D (2017) Twentieth-century atmospheric river activity along the west coasts of Europe and North America: algorithm formulation, reanalysis uncertainty and links to atmospheric circulation patterns. Climate Dynamics 48:2771–2795

Burn DH, Whitfield PH (2018) Changes in flood events inferred from centennial length streamflow data records. Advances in Water Resources 121:333–349

Champion AJ, Allan RP, Lavers DA (2015) Atmospheric rivers do not explain UK summer extreme rainfall. Journal of Geophysical Research: Atmospheres 120:6731–6741

Coles S, Bawa J, Trenner L, Dorazio P (2001) An introduction to statistical modeling of extreme values. Springer

Dhakal N, Jain S, Gray A, et al (2015) Nonstationarity in seasonality of extreme precipitation: A nonparametric circular statistical approach and its application. Water Resources Research 51:4499–4515

Hart RE, Grumm RH (2001) Using normalized climatological anomalies to rank synoptic-scale events objectively. Monthly weather review 129:2426–2442

Knippertz P, Wernli H, Gläser G (2013) A global climatology of tropical moisture exports. Journal of Climate 26:3031–3045

Laaha G, Blöschl G (2006) Seasonality indices for regionalizing low flows. Hydrological Processes: An International Journal 20:3851–3878

Mardia KV (1975) Statistics of directional data. Journal of the Royal Statistical Society: Series B (Methodological) 37:349–371

Pathak A, Ghosh S, Martinez JA, et al (2017) Role of Oceanic and Land Moisture Sources and Transport in the Seasonal and Interannual Variability of Summer Monsoon in India. Journal of Climate 30:1839–1859. https://doi.org/10.1175/JCLI-D-16-0156.1

Poulin A, Huard D, Favre A-C, Pugin S (2007) Importance of tail dependence in bivariate frequency analysis. Journal of Hydrologic Engineering 12:394–403

Salvadori G, Durante F, Perrone E (2013) Semi-parametric approximation of Kendall’s distribution function and multivariate Return Periods. Journal de la société française de statistique 154:151–173